Author's Post-print version. Article published in Chemical Engineering Science
DOI: doi.org/10.1016/j.ces.2013.03.038
Published version: https://www.sciencedirect.com/science/article/pii/S0009250913002200

# Influence of drag force correlations on periodic fluidization behavior in Eulerian-Lagrangian simulation of a bubbling fluidized bed

Xiaoke Ku*, Tian Li and Terese Løvås

Department of Energy and Process Engineering

Norwegian University of Science and Technology (NTNU)

7491 Trondheim, Norway

## ABSTRACT

In this paper, an Eulerian-Lagrangian approach, in which the gas flow is solved by the volume-averaged Navier-Stokes equation and the motion of individual particles is obtained by directly solving Newton's second law of motion, is developed within the OpenFOAM framework to investigate the effects of three well-known inter-phase drag force correlations (Gidaspow 1994, Di Felice 1994 and EHKL 2006) on the fluidization behavior in a bubbling fluidized bed reactor. The inter-particle and particle-wall collisions are modeled by a soft-sphere model which expresses the contact forces with the use of a spring, dashpot and friction slider. The simulation results are analyzed in terms of particle flow pattern, bed expansion, bed pressure drop and fluctuation frequency. Qualitatively, formation of bubbles and slugs and the process of particle mixing are observed to occur for all the drag models, although the Gidaspow model is found to be most energetic and the Di Felice and EHKL models yield minor difference. The flow behavior also shows a strong dependency on the restitution coefficient $e$ and the friction coefficient $\mu$ and no bubbling and slugging occur at all for the ideal-collision case ($e$ = 1, $\mu$= 0). Quantitatively, the mean pressure drops predicted by the three models agree quite well with each other and the amplitudes of the fluctuations measured by the standard deviation are also comparable. However, a significant difference in fluctuation frequency is found and the Gidaspow model

* Corresponding author. Tel.: +47 73593919. E-mail address: xiaoke.ku@ntnu.no (X. Ku).

Author's Post-print version. Article published in Chemical Engineering Science
DOI: doi.org/10.1016/j.ces.2013.03.038
Published version: https://www.sciencedirect.com/science/article/pii/S0009250913002200

predicts a lowest fluctuation frequency whereas the Di Felice model gets a highest one. Finally, effects of the spring stiffness and the discontinuity in the Gidaspow model are studied. The results show that both mean bed pressure drop and fluctuation frequency slightly decrease as the spring stiffness increases for all the three drag models and no significant differences are observed in the mean bed pressure drop and fluctuation frequency between the Gidaspow model and the linear continuous model.

**Keywords:** Particle; Multiphase flow; Drag correlations; Fluidization; Simulation; Fluctuation frequency

## 1. Introduction

Gas-solid fluidized bed reactors are widely used in many industrial operations, such as gasification, combustion, catalytic cracking and various other chemical and metallurgical processes. Some of the compelling advantageous features of fluidized bed reactors are good mixing properties, high particle heating rates, and high reaction rates between gas and solids due to large gas-particle contact area. A good understanding of the hydrodynamic behavior of this system is important for the design and scale up of the new efficient reactors. Thus, in the last two decades significant research efforts have been devoted to the development of numerical models to study the complex hydrodynamics of gas-solid flows in fluidized bed reactors (see, among many others, Esmaili and Mahinpey, 2011; Hoomans et al., 2000; Kafui et al., 2002; Loha et al., 2012; Tsuji et al., 1993).

Generally, all the modeling methods developed can be broadly categorized into Eulerian-Eulerian and Eulerian-Lagrangian approaches. For Eulerian-Eulerian approach, both particle and fluid phases are treated as interpenetrating continua with appropriate interaction terms representing the coupling between the phases. It can predict the macroscopic characteristics of a system with relatively low computational cost and has actually dominated the modeling of fluidization process for many years (Gerber et al. 2010; Taghipour et al., 2005).

Author's Post-print version. Article published in Chemical Engineering Science
DOI: doi.org/10.1016/j.ces.2013.03.038
Published version: https://www.sciencedirect.com/science/article/pii/S0009250913002200

However, in addition to the difficulty of providing closure models for mass exchange or inter-phase interaction within its continuum framework, Eulerian-Eulerian approach is unable to model the flow characteristics of individual particles. On the other hand, for Eulerian-Lagrangian approach which is sometimes called Discrete Element Method (DEM) (Cundall and Strack, 1979), the gas is treated as continuous and particle as discrete phase. The trajectories of individual particles are tracked in space and time by directly integrating the equations of motion while accounting for interactions with other particles, walls and the continuous phase. For dense particle system with multiple contacts between particles the soft-sphere collision model is usually applied. Eulerian-Lagrangian/DEM approach can offer detailed microscopic information, such as trajectories of individual particles and transient forces acting on each particle, which is extremely difficult, even impossible to obtain by macroscopic models or experiments (Jung and Gidaspow, 2005). The use of DEM for fluidized bed modeling was pioneered by Tsuji et al. (1993) and since then, thanks to the dramatic increase in computational capacity, DEM has come more and more into the focus of engineers and researchers (Lin et al., 2003; Papadikis et al., 2009; Su et al., 2011; Zhou et al., 2008).

For both Eulerian-Eulerian and Eulerian-Lagrangian approaches, a key consideration is the coupling between the phases. From a physical point of view, the coupling currently comprises the effect of (a) volume displacement by the particles, and (b) fluid-solid interaction forces exerted on the particles. These non-linear fluid-solid interaction forces or called generalized drag forces are believed to play a very important role in the formation of heterogeneous flow structures in dense gas-fluidized beds (Li and Kuipers, 2003). There are various drag correlations available in the literature. The Gidaspow correlation (Gidaspow, 1994) is a combination of the Ergun equation (Ergun, 1952) for dense granular regime (porosity $\varepsilon_g<0.8$) and the Wen and Yu equation (Wen and Yu, 1966) for dilute granular regime ($\varepsilon_g>=0.8$). This model is often used in the literature, but the transition between the two regimes is discontinuous, which may lead to convergence problems (Kloss

Author's Post-print version. Article published in Chemical Engineering Science
DOI: doi.org/10.1016/j.ces.2013.03.038
Published version: https://www.sciencedirect.com/science/article/pii/S0009250913002200

et al., 2009). Di Felice (1994), using an empirical fit to a wide range of fixed and suspended-particle systems covering the full practical range of flow regimes and porosities, proposed a continuous single-function correlation for the drag force. More recently, Hill et al. (2001a, b) proposed a Hill-Koch-Ladd (HKL) correlation applicable to different ranges of Reynolds numbers and solids volume fractions based on data from Lattice-Boltzmann simulations. Later Benyahia et al. (2006) blended HKL correlation with known limiting forms of the gas-solids drag function and constructed a extended HKL drag correlation (EHKL) which is applicable to the full range of solids volume fractions and Reynolds numbers. Although some works have investigated the effects of different drag models within the Eulerian-Eulerian framework under very different conditions from ours (Du et al, 2006; Esmaili and Mahinpey, 2011; Loha et al., 2012), few are reported for Eulerian-Lagrangian approach (Li and Kuipers, 2003). In our earlier paper (Ku et al, in press), we reported some preliminary results of the qualitative influence of various drag models on the fluidization behavior. In this paper, we detailedly present an Eulerian-Lagrangian approach with a soft-sphere collision model for the simulation of a bubbling fluidized bed. The three drag correlations (Gidaspow 1994, Di Felice 1994 and EHKL 2006) as described above are implemented in our model. The simulation results are analyzed both qualitatively and quantitatively in terms of particle flow pattern, bed pressure drop, and fluctuation frequency with a focus on the detailed comparison between the different drag models.

The rest of this paper is organized as follows. In section 2, the equations of motion describing evolution of the spherical particles and gas phase are firstly formulated. Then the three different drag models and the simulation setup are tabulated. In section 3, the numerical results of motion of particles in a bubbling fluidized bed are presented. Here, we first verify our approach by predicting the minimum fluidization velocity and compare our results with data available in the literature. Then we investigate the fluidization behavior and the pressure drop across the bed where the differences between the drag models are highlighted. Finally effects of

Author's Post-print version. Article published in Chemical Engineering Science
DOI: doi.org/10.1016/j.ces.2013.03.038
Published version: https://www.sciencedirect.com/science/article/pii/S0009250913002200

the restitution coefficient $e$, the friction coefficient $\mu$, the spring stiffness $k_n$ and the effect of the discontinuity in the Gidaspow model are also documented. A short summary and conclusions are given in section 4.

## 2. Mathematical modeling

### *2.1. Discrete particle phase*

A particle in a gas-solid system undergoes translational and rotational motions as described by Newton's second law of motion. The equation governing the translational motion of particle $i$, which reads in a quiescent frame and in dimensional form, is

$$m_i \frac{d\mathbf{v}_i}{dt} = \mathbf{f}_{\mathrm{g},i} + \mathbf{f}_{\mathrm{c},i} + m_i\mathbf{g} \qquad (1)$$

where $m_i$ and $\mathbf{v}_i$ are, respectively, the mass and velocity of particle $i$, and $\mathbf{g}$ is the gravitational acceleration. $\mathbf{f}_{\mathrm{g},i}$ is the total fluid-particle drag force on the particle $i$ including viscous drag force and pressure gradient force in the current case (Hill et al. 2001a,b; Kafui et al., 2002; van der Hoef et al., 2005), and $\mathbf{f}_{\mathrm{c},i}$ is the total force on the particle $i$ due to inter-particle or particle-wall contacts. Note that in the above force balance the added mass effects, Saffman lift force and Basset history force have been neglected, because they play a minor role for the type of flows considered here (Hoomans et al., 1996), as well as the buoyancy force which is allowed because of the negligible density of the gas phase with respect to the density of the particles.

The equation governing the rotational motion of particle $i$ is

$$I_i \frac{d\boldsymbol{\omega}_i}{dt} = \mathbf{T}_i \qquad (2)$$

where $\boldsymbol{\omega}_i$ is the angular velocity, $\mathbf{T}_i$ is the torque arising from the tangential components of the contact forces, and $I_i$ is the moment of inertia, given as $I_i = \frac{2}{5} m_i R_i^2$ for spherical particles with radius $R_i$.

Author's Post-print version. Article published in Chemical Engineering Science
DOI: doi.org/10.1016/j.ces.2013.03.038
Published version: https://www.sciencedirect.com/science/article/pii/S0009250913002200

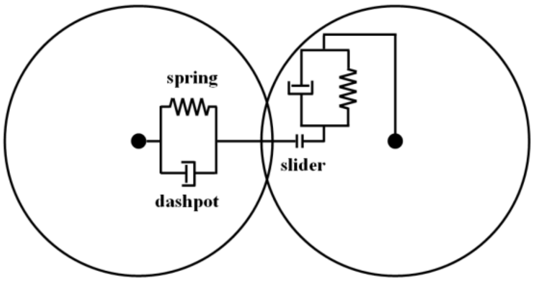


**Fig. 1.** The spring-slider-dashpot model.

Particle-to-particle collision models can be generally classified as hard-sphere or soft-sphere models. In the hard-sphere model, the particles are assumed to be rigid spheres, and collisions among particles are treated as binary, instantaneous and impulsive events. The collisions are processed one by one according to the order in which the events occur. One advantage of the hard-sphere model is that there is an analytical solution available for the collision model. Given the velocities of the particles prior to collision together with the particle properties the post-collision velocities can be calculated exactly. The hard-sphere model is more suitable for simulations of dilute or rapid granular flows since it considers two-body collisions only. However, at high particle number densities, the hard sphere model may break down with long inter-particle contact durations. For further details on the implementation of the hard-sphere model the interested reader is referred to the works of Hoomans et al. (1996, 1999, 2000) and Deen et al. (2007).

Most of the commonly observed gas-solid flows are dense particle systems and exhibit multiple-particle and long-duration contacts. The soft sphere model, which is proposed by Cundall and Strack (1979), is the most applicable in such regimes and also adopted in this paper. In the soft-sphere model, the inter-particle contact forces, namely, the normal, sliding and damping forces, are computed using equivalent simple mechanical elements, such as spring, slider and dashpot (as shown in Fig. 1). The particles are allowed to overlap slightly. The normal force tending to repulse the particles can then be deduced from this spatial overlap and the normal relative velocity at the contact point. The spring stiffness $k_n$ can be calculated by Hertzian contact theory when the physical properties such as Young's modulus and Poisson ratio are known. Particle-wall interactions are treated in the same way as particle-particle interactions except that the walls are assumed to be massive. Concerning the wall properties such as restitution and friction coefficients, the same values as the particle could apply. The net contact force $\mathbf{f}_{c,i}$ and torque $\mathbf{T}_i$ acting on each particle result from a vector summation of the forces and torques at each particle-particle or particle-wall contact. A characteristic feature of the soft particle models is that they are capable of handling multiple particle-particle contacts which is of importance when modeling dense particle systems. Moreover, non-contact force can also be incorporated into soft-sphere model easily. Detailed implementation issues of the soft-sphere model are available in the literature (e.g. Tsuji et al., 1992), which are not stated here for the sake of shortness.

### *2.2. Continuous gas phase*

The continuum gas phase hydrodynamics are calculated from the continuity and volume-averaged Navier-Stokes equations which are coupled with those of the particle phase through the porosity and the inter-phase momentum exchange (Kafui et al., 2002).

The continuity equation is as follows:

$$\frac{\partial}{\partial t}(\varepsilon_{\mathrm{g}}\rho_{\mathrm{g}}) + \nabla\cdot(\varepsilon_{\mathrm{g}}\rho_{\mathrm{g}}\mathbf{u}_{\mathrm{g}}) = 0 \tag{3}$$

and the momentum equation is given by

$$\frac{\partial}{\partial t}(\varepsilon_{\mathrm{g}}\rho_{\mathrm{g}}\mathbf{u}_{\mathrm{g}}) + \nabla\cdot(\varepsilon_{\mathrm{g}}\rho_{\mathrm{g}}\mathbf{u}_{\mathrm{g}}\mathbf{u}_{\mathrm{g}}) = -\nabla p + \nabla\cdot(\varepsilon_{\mathrm{g}}\boldsymbol{\tau}_{\mathrm{g}}) + \varepsilon_{\mathrm{g}}\rho_{\mathrm{g}}\mathbf{g} - \mathbf{S}_{\mathrm{p}} \tag{4}$$

Here, $\varepsilon_{\mathrm{g}}$ is the porosity, and $\rho_{\mathrm{g}}$, $\mathbf{u}_{\mathrm{g}}$, $\boldsymbol{\tau}_{\mathrm{g}}$ and $p$ are the density, velocity, viscous stress tensor and pressure of the gas phase, respectively. $\mathbf{S}_{\mathrm{p}}$ is a source term that describes the momentum exchange of the gas with the solid particles and will be discussed in more detail below. $\boldsymbol{\tau}_{\mathrm{g}}$ is assumed to obey the general form for a Newtonian fluid (Bird et al., 1960),

Author's Post-print version. Article published in Chemical Engineering Science
DOI: doi.org/10.1016/j.ces.2013.03.038
Published version: https://www.sciencedirect.com/science/article/pii/S0009250913002200

$$\boldsymbol{\tau}_g = (\lambda_g - \frac{2}{3}\mu_g)(\nabla \cdot \mathbf{u}_g)\mathbf{I} + \mu_g((\nabla \mathbf{u}_g) + (\nabla \mathbf{u}_g)^{\mathrm{T}}) \tag{5}$$

where the bulk viscosity $\lambda_g$ can be set to zero for gas, $\mu_g$ is the dynamic gas viscosity, and **I** is the identity tensor. The porosity $\varepsilon_g$, which denotes the fraction of a cell volume occupied by gas, is determined by

$$\varepsilon_g = 1 - \frac{\sum_{i=1}^{k_c} V_i}{\Delta V_{cell}} \tag{6}$$

where $V_i$ is the volume of particle $i$ and $k_c$ is the number of particles in the computational cell with volume $\Delta V_{\mathrm{cell}}$.

As the fluid drag force acting on each particle $\mathbf{f}_{g,i}$ is known (see Section 2.1), according to Newton's third law of motion, the volumetric fluid-particle interaction force, $\mathbf{S}_p$, in a computational cell can be obtained by summing up the fluid forces $\mathbf{f}_{g,i}$ acting on all the particles in a fluid cell and dividing by the volume of the fluid cell $\Delta V_{\mathrm{cell}}$, thus

$$\mathbf{S}_p = \frac{1}{\Delta V_{\mathrm{cell}}} \sum_{\forall i \in \mathrm{cell}} \mathbf{f}_{g,i} \tag{7}$$

### *2.3. Drag models*

The fluid drag force acting on particle $i$, $\mathbf{f}_{g,i}$, can be conventionally expressed as follows,

$$\mathbf{f}_{g,i} = \frac{V_i \beta}{\varepsilon_p}(\mathbf{u}_g - \mathbf{v}_i) \tag{8}$$

where $\mathbf{u}_g$ is the instantaneous gas velocity at the particle position, $\varepsilon_p = 1 - \varepsilon_g$, and $\beta$ is the inter-phase momentum transfer coefficient. Three correlations for calculating $\beta$ are summarized in Table 1.

**Table 1**

Three drag correlations proposed for particulate flows

**1. Gidaspow model (1994)**

$$\beta = \begin{cases} 150\dfrac{\varepsilon_{\mathrm{p}}^2\mu_{\mathrm{g}}}{\varepsilon_{\mathrm{g}}^2 d_{\mathrm{p}}^2} + 1.75\dfrac{\varepsilon_{\mathrm{p}}\rho_{\mathrm{g}}}{\varepsilon_{\mathrm{g}} d_{\mathrm{p}}}\left|\mathbf{u}_{\mathrm{g}} - \mathbf{v}_{\mathrm{p}}\right| & \varepsilon_{\mathrm{g}} < 0.8 \\ \dfrac{3}{4} C_d \dfrac{\varepsilon_{\mathrm{p}}\rho_{\mathrm{g}}}{d_{\mathrm{p}}}\left|\mathbf{u}_{\mathrm{g}} - \mathbf{v}_{\mathrm{p}}\right| \varepsilon_{\mathrm{g}}^{-2.65} & \varepsilon_{\mathrm{g}} \geq 0.8 \end{cases}$$

$$C_d = \begin{cases} \dfrac{24}{Re_{\mathrm{p}}}(1 + 0.15 Re_{\mathrm{p}}^{0.687}) & Re_{\mathrm{p}} < 1000 \\ 0.44 & Re_{\mathrm{p}} \geq 1000 \end{cases}$$

$$Re_{\mathrm{p}} = \varepsilon_{\mathrm{g}}\rho_{\mathrm{g}} d_{\mathrm{p}}\left|\mathbf{u}_{\mathrm{g}} - \mathbf{v}_{\mathrm{p}}\right| / \mu_{\mathrm{g}}$$

**2. Di Felice model (1994)**

$$\beta = \frac{3}{4} C_d \frac{\varepsilon_{\mathrm{p}}\varepsilon_{\mathrm{g}}\rho_{\mathrm{g}}}{d_{\mathrm{p}}}\left|\mathbf{u}_{\mathrm{g}} - \mathbf{v}_{\mathrm{p}}\right| \varepsilon_{\mathrm{g}}^{-\chi}$$

$$C_d = (0.63 + \frac{4.8}{\sqrt{Re_{\mathrm{p}}}})^2 \quad \chi = 3.7 - 0.65\exp\left[-\frac{(1.5 - \log_{10}(Re_{\mathrm{p}}))^2}{2}\right]$$

$$Re_{\mathrm{p}} = \varepsilon_{\mathrm{g}}\rho_{\mathrm{g}} d_{\mathrm{p}}\left|\mathbf{u}_{\mathrm{g}} - \mathbf{v}_{\mathrm{p}}\right| / \mu_{\mathrm{g}}$$

**3. EHKL model (2006)**

$$\beta = \frac{18\mu_{\mathrm{g}}\varepsilon_{\mathrm{g}}\varepsilon_{\mathrm{p}}}{d_{\mathrm{p}}^2} F$$

$$\begin{cases} F = 1 + 3/8 Re_{\mathrm{p}}, & \varepsilon_{\mathrm{p}} \leq 0.01 \text{ and } Re_{\mathrm{p}} \leq (F_2 - 1)/(3/8 - F_3) \\ F = F_0 + F_1 Re_{\mathrm{p}}^2, & \varepsilon_{\mathrm{p}} > 0.01 \text{ and } Re_{\mathrm{p}} \leq (F_3 + \sqrt{F_3^2 - 4F_1(F_0 - F_2)})/(2F_1) \\ F = F_2 + F_3 Re_{\mathrm{p}}, & \text{otherwise} \end{cases}$$

$$F_0 = \begin{cases} (1-w)\dfrac{1 + 3\sqrt{\varepsilon_{\mathrm{p}}/2} + (135/64)\varepsilon_{\mathrm{p}}\ln(\varepsilon_{\mathrm{p}}) + 17.14\varepsilon_{\mathrm{p}}}{1 + 0.681\varepsilon_{\mathrm{p}} - 8.48\varepsilon_{\mathrm{p}}^2 + 8.16\varepsilon_{\mathrm{p}}^3} + \mathrm{w}\dfrac{10\varepsilon_{\mathrm{p}}}{\varepsilon_{\mathrm{g}}^3} & 0.01 < \varepsilon_{\mathrm{p}} < 0.4 \\ 10\varepsilon_{\mathrm{p}}/\varepsilon_{\mathrm{g}}^3 & \varepsilon_{\mathrm{p}} \geq 0.4 \end{cases}$$

$$F_1 = \begin{cases} \sqrt{2/\varepsilon_{\mathrm{p}}}/40 & 0.01 < \varepsilon_{\mathrm{p}} \leq 0.1 \\ 0.11 + 0.00051 e^{11.6\varepsilon_{\mathrm{p}}} & \varepsilon_{\mathrm{p}} > 0.1 \end{cases}$$

$$F_2 = \begin{cases} (1-w)\dfrac{1 + 3\sqrt{\varepsilon_{\mathrm{p}}/2} + (135/64)\varepsilon_{\mathrm{p}}\ln(\varepsilon_{\mathrm{p}}) + 17.89\varepsilon_{\mathrm{p}}}{1 + 0.681\varepsilon_{\mathrm{p}} - 11.03\varepsilon_{\mathrm{p}}^2 + 15.41\varepsilon_{\mathrm{p}}^3} + \mathrm{w}\dfrac{10\varepsilon_{\mathrm{p}}}{\varepsilon_{\mathrm{g}}^3} & \varepsilon_{\mathrm{p}} < 0.4 \\ 10\varepsilon_{\mathrm{p}}/\varepsilon_{\mathrm{g}}^3 & \varepsilon_{\mathrm{p}} \geq 0.4 \end{cases}$$

$$F_3 = \begin{cases} 0.9351\varepsilon_{\mathrm{p}} + 0.03667 & \varepsilon_{\mathrm{p}} < 0.0953 \\ 0.0673 + 0.212\varepsilon_{\mathrm{p}} + 0.0232/\varepsilon_{\mathrm{g}}^5 & \varepsilon_{\mathrm{p}} \ge 0.0953 \end{cases}$$

$$Re_{\mathrm{p}} = \varepsilon_{\mathrm{g}}\rho_{\mathrm{g}}d_{\mathrm{p}}\left|\mathbf{u}_{\mathrm{g}} - \mathbf{v}_{\mathrm{p}}\right|/(2\mu_{\mathrm{g}}) \qquad w = e^{(-10(0.4-\varepsilon_{\mathrm{p}})/\varepsilon_{\mathrm{p}})}$$

As shown in Table 1, the Gidaspow model combines the Ergun (1952) and Wen and Yu (1966) correlations for the dilute and dense granular regime where a porosity $\varepsilon_{\mathrm{g}}$ of 0.8 is adopted as the boundary between these two regimes. This model is very common, but the step change inherent in the calculated drag forces at a porosity of 0.8 may be not good from a numerical point of view (Kafui et al., 2002). Di Felice (1994), using an empirical fit to a wide range of fixed and suspended-particle systems covering the full practical range of particle Reynolds number $Re_{\mathrm{p}}$ and $\varepsilon_{\mathrm{g}}$, proposed a continuous single-function correlation for the drag force on a particle in a multi-particle system (Di Felice Model). Hill et al. (2001a, b) proposed a set of drag correlations applicable to different ranges of $Re_{\mathrm{p}}$ and solids volume fractions $\varepsilon_{\mathrm{p}}$, based on data from Lattice-Boltzmann simulations. These correlations do not cover the full range of $Re_{\mathrm{p}}$ and $\varepsilon_{\mathrm{p}}$ encountered in fluidized bed simulations. Later Benyahia et al. (2006) blended the Hill-Koch-Ladd (HKL) drag correlations with known limiting forms of the gas-solids drag function such that the blended function (EHKL model) is continuous with respect to $Re_{\mathrm{p}}$ and $\varepsilon_{\mathrm{p}}$. Note that, in EHKL model, $Re_{\mathrm{p}}$ is based on particle radius, rather than particle diameter.

### *2.4. Computational methodology*

Since the governing equations for the gas phase and the particle phase are different, different solution schemes have to be used. For discrete particle simulations, a first-order Euler time integration scheme is used to solve the translational and rotational motions of particles. For continuous gas phase, the governing equations are discretized in finite volume form and solved with a standard pressure based PISO (pressure implicit splitting of operators) solver for variable density flow. The coupling between the discrete particles and the gas phase is numerically achieved as follows. At each time step, the discrete particle equations of motion are first solved yielding the positions $\mathbf{r}_i$ and velocities $\mathbf{v}_i$ of individual particles. This enables the porosity $\varepsilon_g$ and volumetric fluid-particle interaction force $\mathbf{S}_p$ of each computational cell to be calculated. Using the known values of $\varepsilon_g$ and $\mathbf{S}_p$ at the current time, the gas-phase hydrodynamic equations are next solved to give the gas velocity and pressure fields from which the fluid drag forces $\mathbf{f}_{g,i}$ and torque $\mathbf{T}_i$ acting on individual particles are calculated. Using the $\mathbf{f}_{g,i}$ and $\mathbf{T}_i$ will produce information about the motion of individual particles for the next time step. All the above schemes have been developed and implemented into an open source C++ toolbox OpenFOAM (OpenCFD Ltd, 2011). Within the OpenFOAM framework, one can customize solvers or extend the numerical libraries to their own needs relatively easily which is a major advantage over commercial software. The codes are used in a variety of scientific applications, and there are an increasing number of researchers who are using OpenFOAM as their developing platform in their work on topics related to the present work (Oevermann et al., 2009; Su et al., 2011).

### *2.5. Simulation setup*

The simulated fluidized bed geometry as shown schematically in Fig. 2 is similar to those of Tsuji et al. (1993) and Xu and Yu (1997). It consists of a rectangular container of dimension 0.15m (width)×0.9m (height)×0.004m (thickness) with a jet orifice of 0.01 m in width at the centre of the bottom wall. The left, right, bottom walls, the bottom orifice and the top exit consist of the whole calculation domain boundaries. The fluidization solid particles are a group of 2400 spherical particles with a diameter of 4 mm which are also taken from Tsuji et al. (1993) and Xu and Yu (1997). Note that the thickness of the bed is set equal to the particle diameter; that is, the bed contains one layer of particles. Air at a temperature of 293 K and standard atmospheric pressure is used as the fluidizing agent and introduced from the bottom orifice with a uniform velocity. This particle-fluid combination corresponds to a Geldart group D type (Geldart, 1973). Table 2 shows the parameter settings used in the simulation and the boundary conditions for the gas phase are listed in Table 3. Unless stated otherwise, all results of the following sections are based on the settings of Table 2.

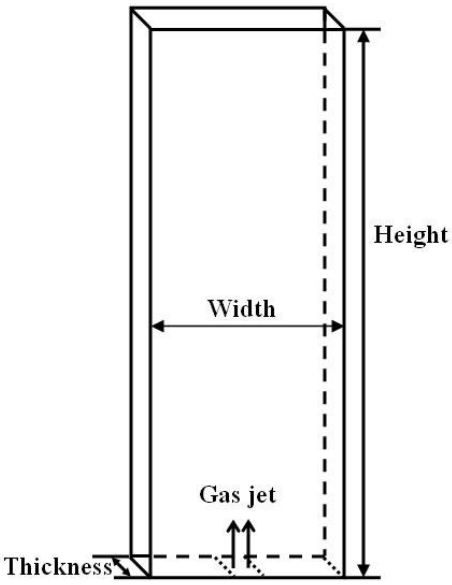


**Fig. 2.** Geometry of the fluidized bed reactor.

The grid resolution employed here is arrived at by a corresponding grid independence study. To seek a proper grid system, four different grid systems of ($\Delta x$, $\Delta y$) = (25mm, 45mm), (15mm, 30mm), (10mm, 20mm) and (5mm, 10mm) are tested. In the test, only air (293 K) with the uniform inlet velocity 0.01 m/s covering the whole bottom section is sent into the reactor. Figure 3 displays the velocity distribution at the top exit of the reactor. It can be seen that the velocity profiles in terms of the third and fourth grid systems coincide with the analytic solution. This implies that the third grid system, i.e. ($\Delta x$, $\Delta y$) = (10mm, 20mm), can satisfy the requirement of grid independence. Moreover, for dense gas-solid flows, the choice of grid size is a little more complex. As is well-known, the grid size should be larger than the particle size for DEM simulations. Wang et al. (2009) concluded that in order to obtain correct bed expansion characteristics, the grid size should be of the order of three particle diameters. Considering the particle diameter is 4mm in our study, ($\Delta x$, $\Delta y$) = (10mm, 20mm) is a good choice which takes both the grid independence and particle size into account. For the grid

Author’s Post-print version. Article published in Chemical Engineering Science
DOI: doi.org/10.1016/j.ces.2013.03.038
Published version: https://www.sciencedirect.com/science/article/pii/S0009250913002200

system of ($\Delta x$, $\Delta y$) = (10mm, 20mm), three small time steps, $1.0\times10^{-4}$, $1.0\times10^{-5}$, and $1.0\times10^{-6}$ s which are consistent with the CFL criterion, are also tested to study the time step independence. No difference in the velocity profiles at the top exit is observed upon switching a time step $1.0\times10^{-5}$ s to a smaller value of $1.0\times10^{-6}$ s. So $1.0\times10^{-5}$ s is chosen for all the simulation cases.

**Table 2**

Parameter settings for the simulations

| **Particles** | | **Gas phase** | | **Bed** | |
|---|---|---|---|---|---|
| Shape | Spherical | Viscosity, $\mu_g$ | $1.8\times10^{-5}$ Pa.s | Width | 0.15 m |
| Diameter, $d_p$ | 4 mm | Density, $\rho_g$ | * | Height | 0.9 m |
| Density, $\rho_p$ | 2700 kg/m$^3$ | Temperature, $T$ | 293 K | Thickness | 4 mm |
| Number, $N_p$ | 2400 | Fluid time step, $\Delta t$ | $1\times10^{-5}$ s | Cell width, $\Delta x$ | 10 mm |
| Restitution coefficient, $e$ | 0.9 | Inlet jet velocity | 48 m/s | Cell height, $\Delta y$ | 20 mm |
| Friction coefficient, $\mu$ | 0.3 | | | Orifice width | 10 mm |

* $\rho_g$ is determined using the ideal gas law.

**Table 3**

Boundary conditions for gas phase in the simulation.

| **Boundaries** | **Velocity** | **Pressure** | **Porosity** |
|---|---|---|---|
| Left and right walls | No slip | Zero gradient | Zero gradient |
| Bottom wall | No slip | Zero gradient | Zero gradient |
| Inlet orifice (bottom) | Fixed value | Zero gradient | Fixed value |
| Outlet (top) | Zero gradient | Fixed value | Zero gradient |

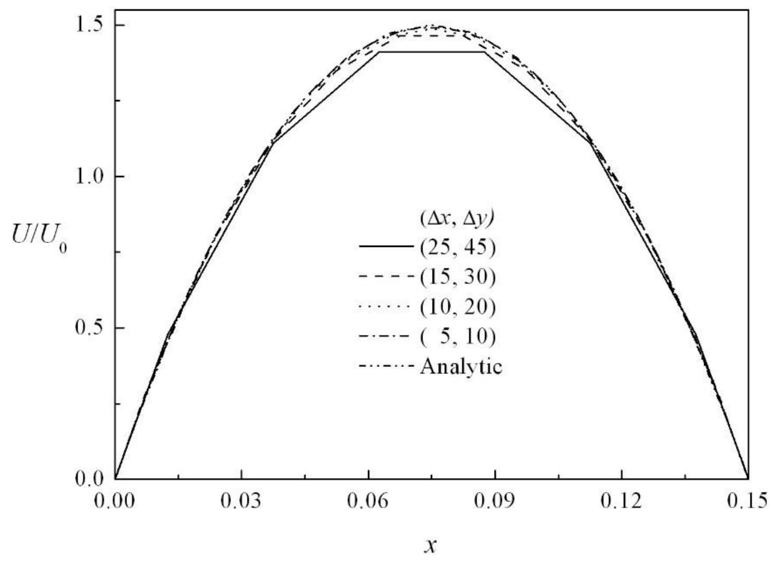


**Fig. 3.** Velocity distribution at the top exit when only air with the uniform inlet velocity $U_0$ =0.01 m/s covering the whole bottom section is sent into the reactor.

## 3. Results and discussions

### *3.1. Bed preparation*

The first step of the fluidization simulation is to obtain an initial bed configuration which is generated as follows. The container is uniformly divided into a set of small rectangular lattices throughout the calculation domain. Then 2400 particles with zero velocity are positioned at the centers of these lattices and allowed to fall down under the influence of gravity in the absence of inlet jet gas. As shown in Fig. 4, pluvial deposition of the particles finally results in a static bed of height about 0.23 m and porosity around 0.42. This deposited bed is then used as the initial input data for the fluidization simulation. As pointed out by Xu and Yu (1997), the initial input data for fluidization include not only the particle coordinates but also the forces and torques which come with the deposition of particles in the packing process.

Author's Post-print version. Article published in Chemical Engineering Science
DOI: doi.org/10.1016/j.ces.2013.03.038
Published version: https://www.sciencedirect.com/science/article/pii/S0009250913002200

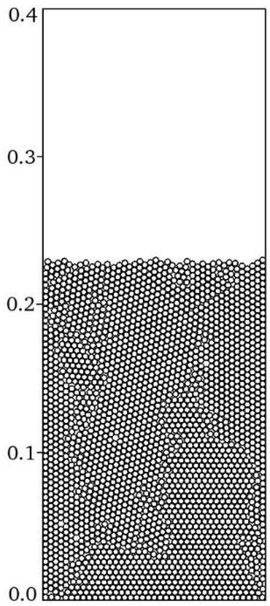


**Fig. 4.** Particle configurations after a simulated packing process.

### *3.2. Minimum fluidization velocity*

To test the validity of our approach, defluidization simulations, which allow the minimum fluidization velocity $\mathbf{u}_{mf}$ to be determined, are performed using each of the three drag correlations formulated in Table 1. As shown in Fig. 5, the defluidization curves are given by the mean pressure drop through the bed, $\Delta\bar{p}$ vs superficial gas velocity $\mathbf{u}_s$. The superficial gas velocity $\mathbf{u}_s$, here as an alternative to the gas jet velocity, is defined as the total volumetric gas flow rate divided by the entire bed cross-sectional area. Totally, 20 runs of simulation are carried out for each drag model, corresponding to the cases with a decreasing $\mathbf{u}_s$. The case for the maximum $\mathbf{u}_s$ of 3.2 m/s is simulated under the same boundary and initial conditions outlined in subsection 3.1. Then the cases corresponding to the decreasing $\mathbf{u}_s$ are simulated by successively decreasing $\mathbf{u}_s$, with the final results at a higher velocity as the initial input data for the simulation at next lower velocity. All the cases are run for 10 s real time for statistical purpose. Two regimes are indentified from the defluidization curves: fluidized bed regime and packed bed regime. As will be delineated in the following subsection, at the fully fluidized bed regime, bubbles and slugs are generated continuously during the gas flow and particles move

Author's Post-print version. Article published in Chemical Engineering Science
DOI: doi.org/10.1016/j.ces.2013.03.038
Published version: https://www.sciencedirect.com/science/article/pii/S0009250913002200

vigorously inside the bed. This regime is characterized by an almost constant mean bed pressure drop $\Delta\bar{p}$. It can be observed that all three drag models predict a complete fluidization at the same level of $\Delta\bar{p}$. The $\Delta\bar{p}$ keeps almost constant with decreasing $\mathbf{u}_s$ until a critical point (minimum fluidization velocity $\mathbf{u}_{mf}$) is reached. After $\mathbf{u}_{mf}$ $\Delta\bar{p}$ starts to continuously decrease with decreasing $\mathbf{u}_s$ and a packed bed regime where no bubbles exist is generated. The dotted horizontal line in Fig. 5 indicates the constant mean pressure drop at fluidized bed regime and it intersects the defluidization curves at point $\mathbf{u}_{mf}$. Table 4 shows the comparison of predicted values of minimum fluidization velocity $\mathbf{u}_{mf}$ by the three drag models with the numerical data reported by other investigators (Boyalakuntla, 2003; Hoomans et al, 1996; Xu and Yu, 1997). It can be seen that good agreement is obtained. Figure 6 depicts the predicted porosity distributions at minimum fluidization velocity $\mathbf{u}_{mf}$ for the three drag models. It is observed that only a small bubble forms at the jet region and the porosity distribution is relatively homogeneous through the bed which indicates that the gas could pass through the bed without resulting in a rigorous particle flow. There are no significant differences in porosity distribution among the three drag models except for the upper surface of the bed.

The $\mathbf{u}_{mf}$ is a key quantity for fluidized bed and the successful prediction of this quantity thereby provides an important example to verify the proposed approach. It should be noted that, although the deviation is not large, Gidaspow model predicts a smallest $\mathbf{u}_{mf}$ while EHKL model gives a largest one.

Author's Post-print version. Article published in Chemical Engineering Science
DOI: doi.org/10.1016/j.ces.2013.03.038
Published version: https://www.sciencedirect.com/science/article/pii/S0009250913002200

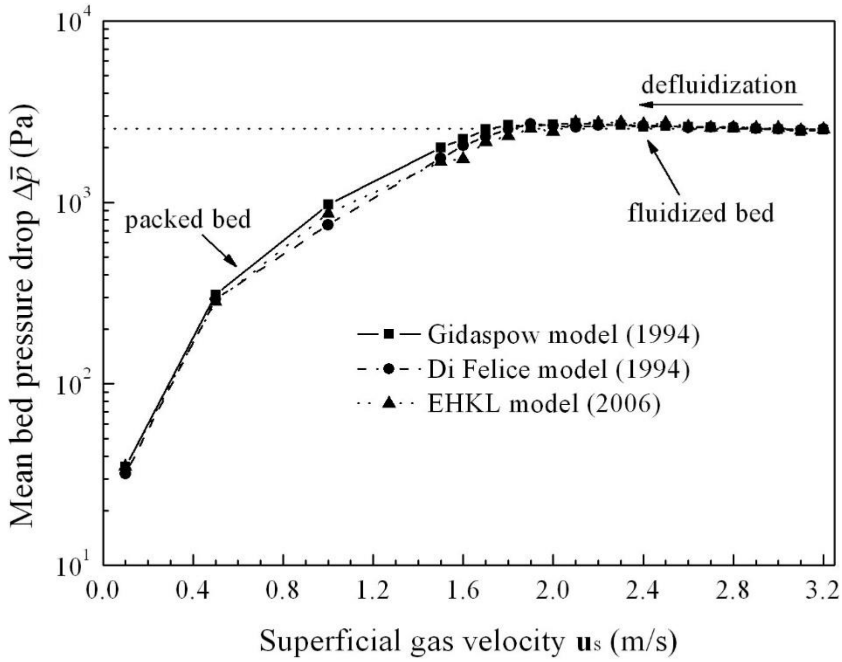


**Fig. 5.** Defluidization curves for the three drag models**.**

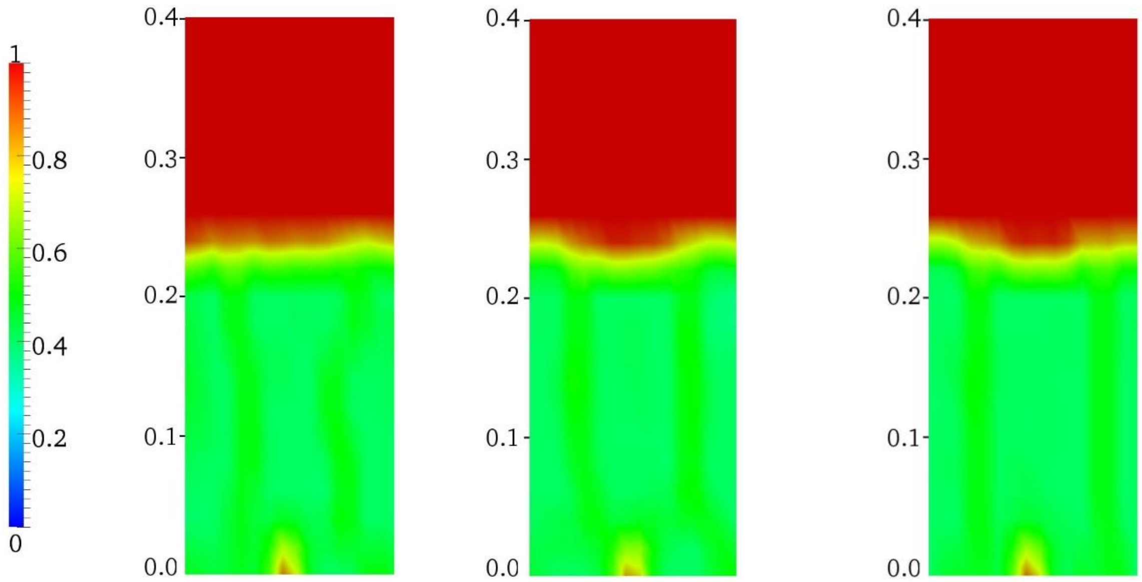

(a) (b) (c)

**Fig. 6.** Simulated porosity distributions at minimum fluidization velocity for the three drag models. (a) Gidaspow model; (b) Di Felice model; (c) EHKL model.

Author's Post-print version. Article published in Chemical Engineering Science
DOI: doi.org/10.1016/j.ces.2013.03.038
Published version: https://www.sciencedirect.com/science/article/pii/S0009250913002200

**Table 4**

Comparison of predicted values of minimum fluidization velocity $\mathbf{u}_{mf}$ by the three drag models with the data reported by other investigators.

| Drag model used | Minimum fluidization velocity $\mathbf{u}_{mf}$ (m/s) | | | |
|---|---|---|---|---|
| | This work | Hoomans et al. (1996) | Xu and Yu (1997) | Boyalakuntla (2003) |
| Gidaspow (1994) | 1.7 | 1.77 | - | 1.85* |
| Di Felice (1994) | 1.8 | - | 1.8 | - |
| EHKL (2006) | 1.9 | - | - | |

* The drag model used by Boyalakuntla (2003) is not explicitly specified in his work.

### *3.3. Fluidization behavior*

Using the particle configurations as shown in Fig. 4 as the initial input, a single central jet of air with velocity of 48 m $s^{-1}$ is injected from the bottom orifice to investigate the fluidization behavior. From detailed examinations of the video sequences of the simulations (available on demand), two ranges are identified: the start-up stage and the fluidization stage. The start-up time range 0.00-0.40 s can be roughly recognized from the first fluctuation of Fig. 11 which depicts the bed pressure drop $\Delta p$ against time $t$ in the following subsection. Figure 7 illustrates the comparison of simulated particle flow patterns using different drag models at the start-up stage. As an initial response of the bed to the introduction of fluidizing gas, a significant upward flow of particles is caused due to the instantaneous breakup of the inter-particle locking. For all models, it is readily observed that a bubble with an oval shape is formed at the jet region, which forces particles in its front to rise and then fall down along the walls. This bubble grows as gas flows upward and eventually collapses. Besides the bubble formation, the existence of "slug" structure at the upper part of the bed is also clearly predicted by all the models. The term "slug" is used here to describe a dilute region of particles which occupies the whole width of the bed and a similar definition is also given by other investigators (Hoomans et al., 1996; Kafui et al., 2002). The formation of bubbles and slugs in a spouting bed of Geldart group D type powder are also reported in the literature both numerically (Boyalakuntla, 2003; Hoomans et al, 1996; Xu and Yu, 1997) and

Author's Post-print version. Article published in Chemical Engineering Science
DOI: doi.org/10.1016/j.ces.2013.03.038
Published version: https://www.sciencedirect.com/science/article/pii/S0009250913002200

experimentally (Tsuji et al., 1993). Although the bubble shape and slug structure are accurately predicted by all the three models, the size of them as well as the height of bed expansion is different. It is easily seen that the Gidaspow model predicts the biggest bubble and slug structure. At $t$ = 0.20 s, a bed expansion estimated at 70% of the initial bed height is observed for the Gidaspow model compared to 50% for the Di Felice model and 40% for the EHKL model.

After the start-up stage, a dynamically stable fluidization stage is reached in which a periodic generation of bubbles and slugs is observed. Figure 8 shows the typical particle flow patterns at this stage for the three drag models. Because the total simulation time is 20 s, a time range which is close to 10 s (half of the total simulation time) is chosen to act as a general representative period for all the models. For each model, five snapshots of the particle patterns show the rise and fall of a bubble which roughly represents a period, which shows that the bubbling period is longest for Gidaspow model and almost same for Di Felice and EHKL models. Similar to the start-up stage, the particle flow patterns predicted by the three models featured by a gas cavity at the jet region above which a bubble is formed and continuously grows and rises until converts to a slug. However, the bubble and slug patterns can differ significantly among the drag models and their intensity is strongest for Gidaspow model and much weaker for De Felice and EHKL models. These observed differences suggest that the performance characteristics obtainable from the different drag models differ, perhaps significantly, depending on the particular application.

Author's Post-print version. Article published in Chemical Engineering Science
DOI: doi.org/10.1016/j.ces.2013.03.038
Published version: https://www.sciencedirect.com/science/article/pii/S0009250913002200

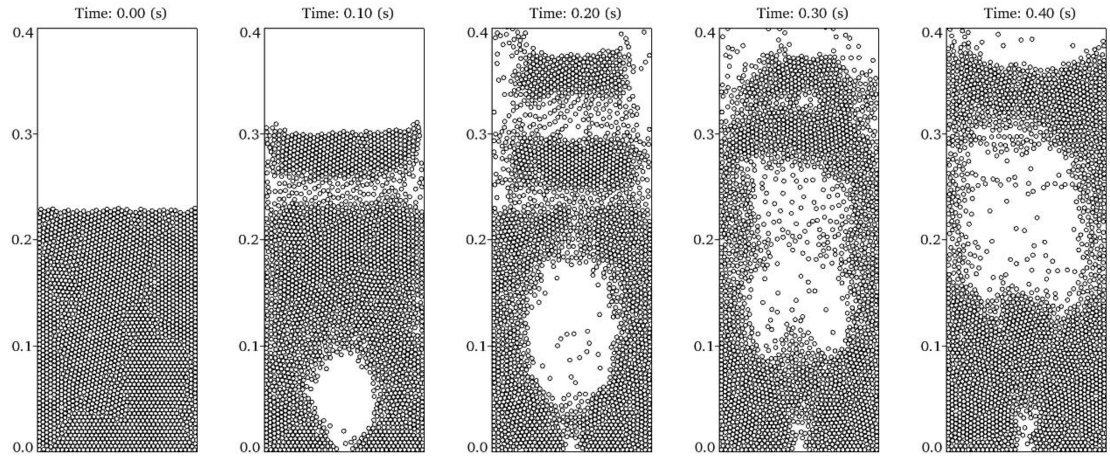


(a)

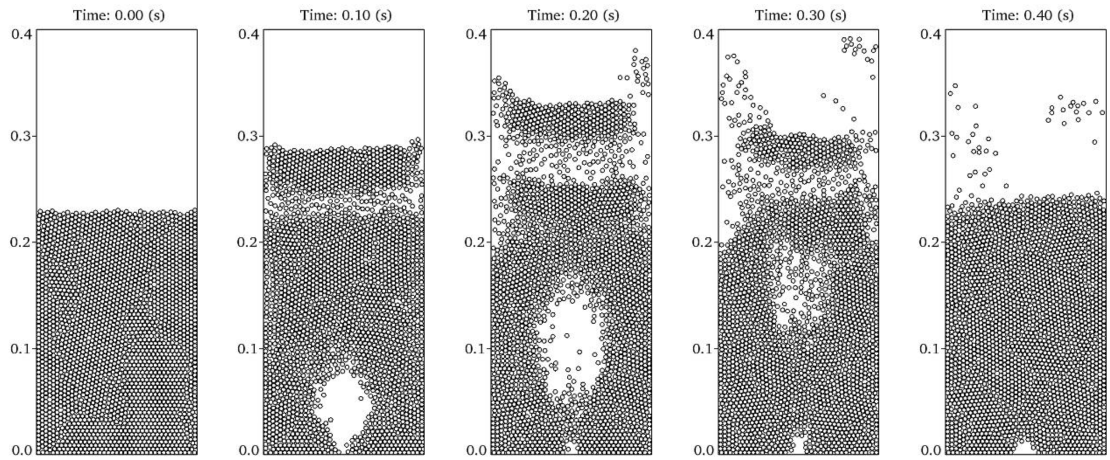


(b)

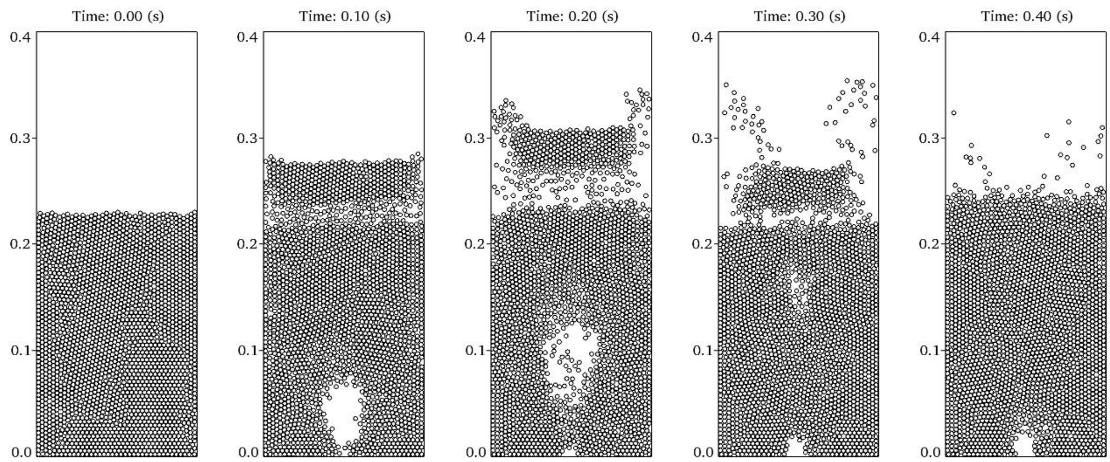


(c)

**Fig. 7.** Particle flow patterns at the start-up stage. (a) Gidaspow model; (b) Di Felice model; (c) EHKL model.

Author's Post-print version. Article published in Chemical Engineering Science
DOI: doi.org/10.1016/j.ces.2013.03.038
Published version: https://www.sciencedirect.com/science/article/pii/S0009250913002200

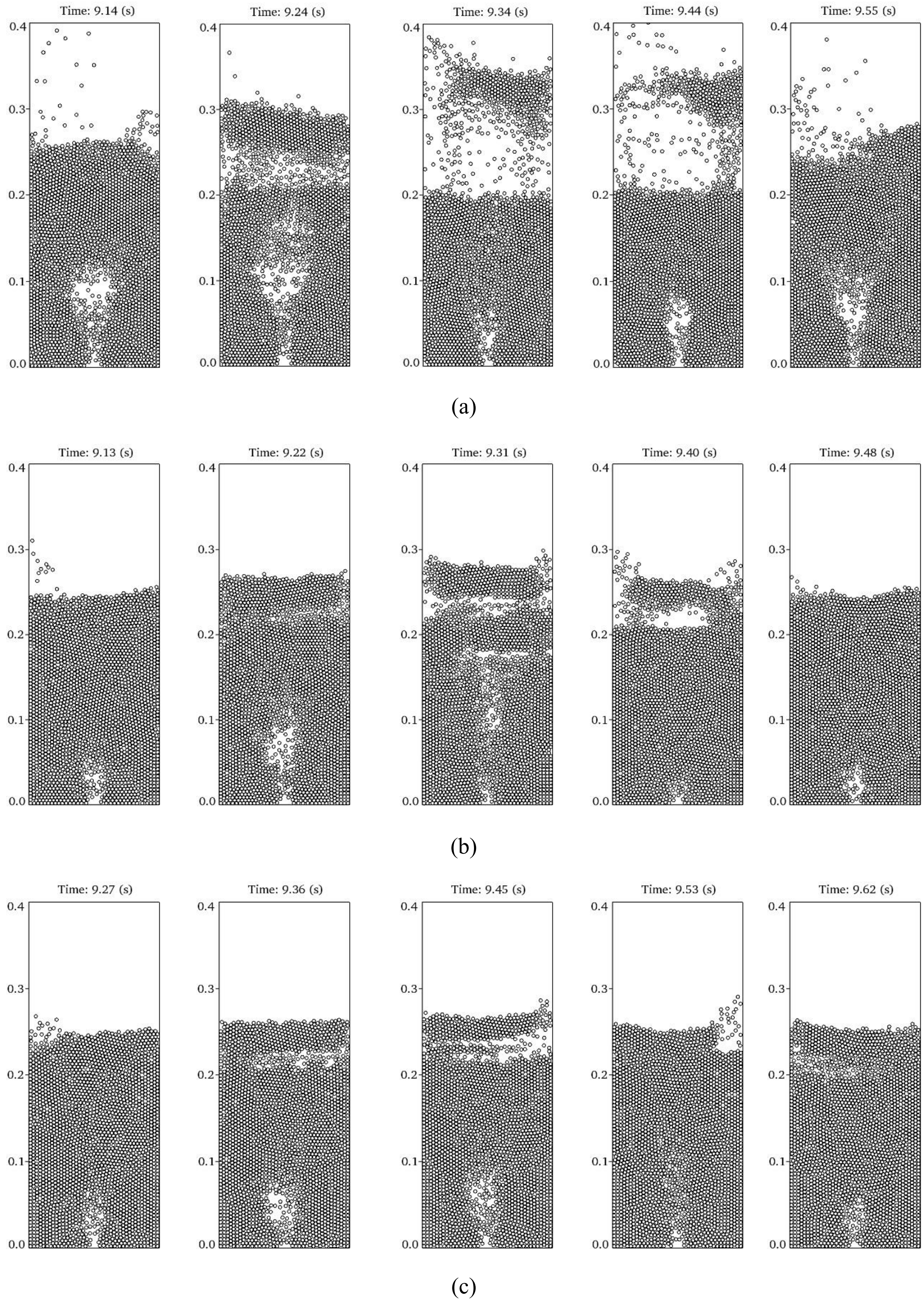


**Fig. 8.** Typical particle flow patterns at the fluidization stage. (a) Gidaspow model; (b) Di Felice model; (c) EHKL model.

Author's Post-print version. Article published in Chemical Engineering Science
DOI: doi.org/10.1016/j.ces.2013.03.038
Published version: https://www.sciencedirect.com/science/article/pii/S0009250913002200

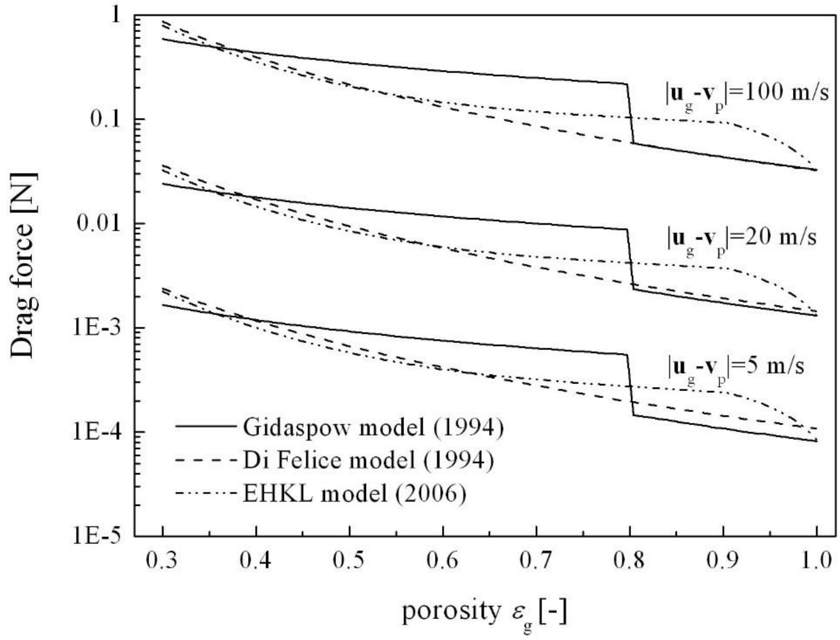


**Fig. 9.** Comparison of drag forces acting on a 4 mm diameter particle as predicted using the Gidaspow model, Di Felice model, and EHKL model for a range of porosities at three superficial slip velocities.

As indicated in Eq. (1), the motion of a particle is governed by the gravitational, fluid drag and inter-particle forces. The fluid drag is closely related to the particle configuration (porosity), gas-solid slip velocity and properties of the gas and the particles. Figure 9 presents plot of the drag forces acting on a single particle for the three drag models as a function of porosity $\varepsilon_g$ at three gas-solid slip velocities $|\mathbf{u}_g-\mathbf{v}_p|$. In the plot the step change inherent in the calculated drag forces from the Gidaspow model at a porosity $\varepsilon_g$ of 0.8 is clearly observed. Three scenarios exist for constant $|\mathbf{u}_g-\mathbf{v}_p|$. First, for $\varepsilon_g$<0.4, De Felice and EHKL models predict drag forces close to each other which are larger than the one produced by Gidaspow model. Second, for $\varepsilon_g$ between 0.4 and 0.8, Gidaspow model gives much larger drag force than De Felice and EHKL models. Finally, for $\varepsilon_g$>0.8, Gidaspow model has a step change and produces a smallest drag force. These trends for the three slip velocities are similar, but the intersections of the curves shift to lower porosities when $|\mathbf{u}_g-\mathbf{v}_p|$ increases. Considering $\varepsilon_g$ ranges from about 0.42 (packed bed as shown in Fig. 4) to 0.96 (only one particle in a fluid cell) for our simulation cases, it is reasonable that Gidaspow model is found to be most energetic as shown in

Figs 7 and 8. Moreover, EHKL and De Felice models intersect at a point around $\varepsilon_g$=0.6 and produce a same level drag force for $\varepsilon_g$<0.8 which is a possible explanation to the similar fluidization behaviors observed for these two models.

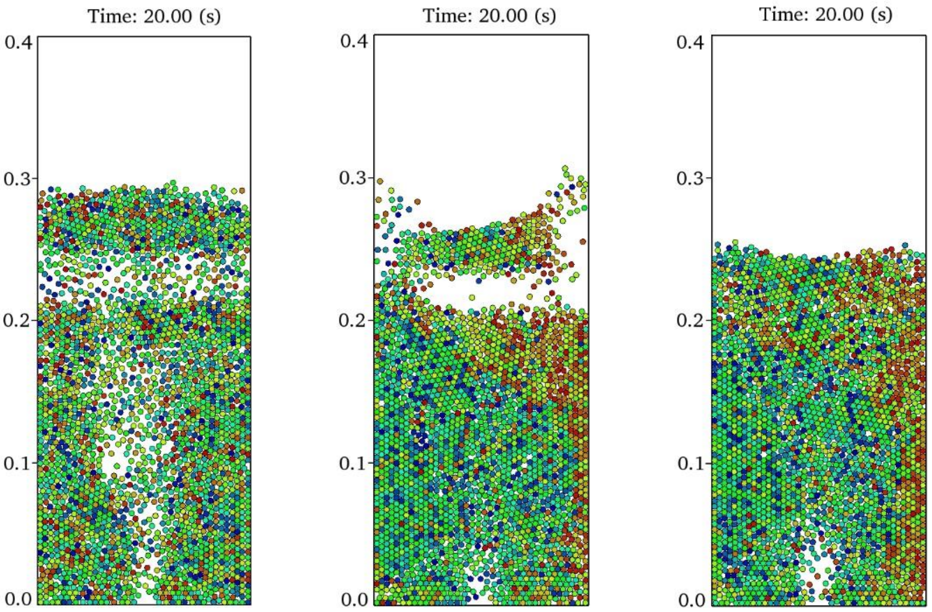


(a) (b) (c)

**Fig. 10.** Degree of mixing at the end of simulation, $t$ = 20 s. (a) Gidaspow model; (b) Di Felice model; (c) EHKL model.

From the fluidization behavior shown in Figs 7 and 8, we know that most of the particle mixing occurs in two fast particle flow regions: one is away from the bottom orifice due to the gas dragging in the main stream (bubble) and the other at the upper part of the bed due to the falling of the particles to fill in the vacant space (slug). There is a big vortex developed corresponding to these two fast flow regions, which promotes particle mixing considerably. However, near the bottom corners the particles become consolidated and mix slowly. If the particles are initially colored in layers gradually changed from blue at bottom to red at top, the degree of mixing at the end of simulation ($t$ = 20 s) for different models are shown in Fig. 10. It is evident that the mixing is best for the Gidaspow model and the particle distribution appears to be uniform throughout the

Author's Post-print version. Article published in Chemical Engineering Science
DOI: doi.org/10.1016/j.ces.2013.03.038
Published version: https://www.sciencedirect.com/science/article/pii/S0009250913002200

bed. Whereas for Di Felice and EHKL models there is still local accumulation of red particles along the right wall and the degree of mixing is comparable for the two models.

### *3.4. Bed pressure drop*

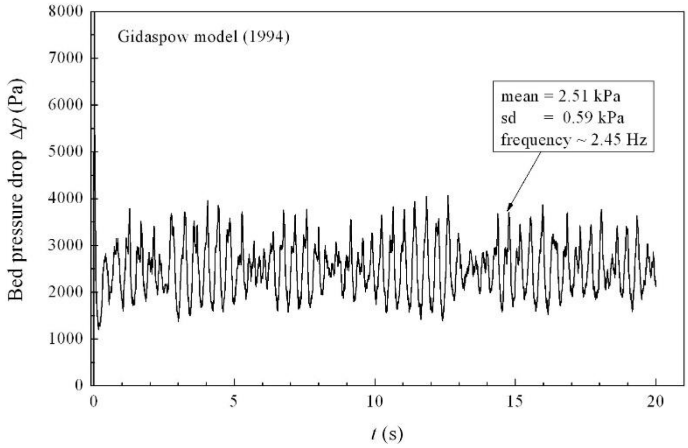


(a)

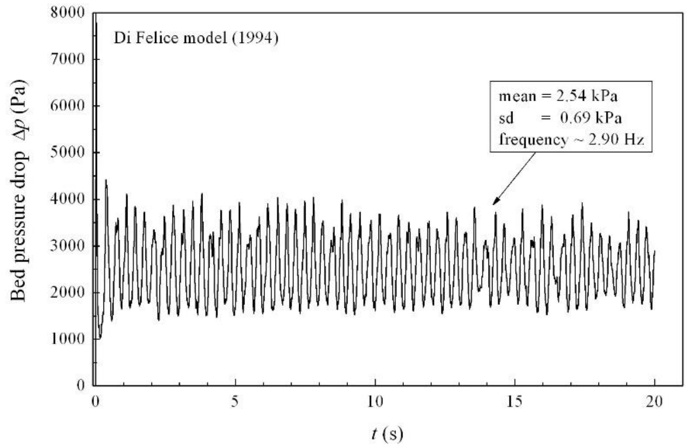


(b)

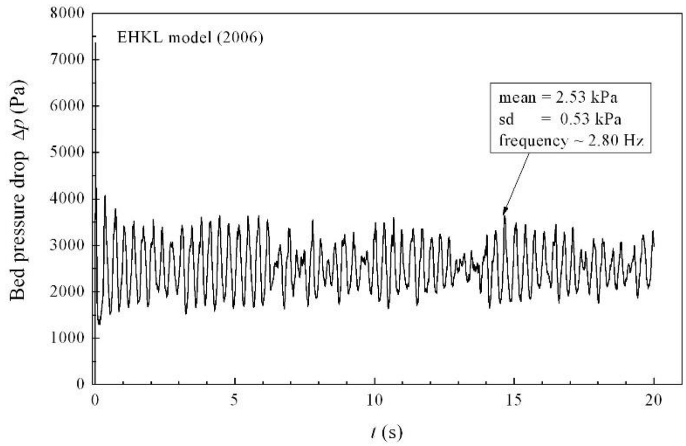


(c)

**Fig. 11.** Bed pressure drop $\Delta p$ against time $t$. (a) Gidaspow model; (b) Di Felice model; (c) EHKL model.

Author's Post-print version. Article published in Chemical Engineering Science
DOI: doi.org/10.1016/j.ces.2013.03.038
Published version: https://www.sciencedirect.com/science/article/pii/S0009250913002200

In the previous subsection, most comparisons between the different drag models are qualitative. In order to quantify the differences, the pressure drop across the bed $\Delta p$, which is obtained as the difference between the average gas pressure in the bottom and top rows of the computational cells, is recorded over a sufficiently long time (20 s) to permit the calculation of a time-averaged value. Figure 11 shows a comparison between all drag models in prediction of $\Delta p$ against time. It is easily seen that $\Delta p$ fluctuates with time and a similar fluctuating pattern is observed for the three drag models. At the start-up stage the bed pressure drop is much higher than that at the stable fluidization stage because of the need to overcome the inter-particle locking. The mean pressure drops of 2.51 kPa, 2.54 kPa and 2.53 kPa for the Gidaspow, Di Felice and EHKL models, respectively, agree quite well with each other and the amplitudes of the fluctuations measured by the standard deviation (sd), are also comparable. However, a significant difference is still evident from Fig. 11 in that Gidaspow model predicts the lowest fluctuation frequency (2.45 Hz), about 85% of what is predicted by the two other models. The frequencies predicted by Di Felice and EHKL models are close to each other, although a slightly higher (~4%) frequency is obtained with Di Felice model.

The bed pressure drop fluctuations in a bubbling fluidized bed are considered to be caused by bubbles and slugs that form and collapse at regular intervals (Boyalakuntla, 2003). From a close inspection of Figs 8 and 11, we see that the pressure fluctuation frequency is in accordance with the bubbling frequency thus supporting the idea that bubbles and slugs are a major cause for the pressure fluctuations. Based on the work of Tho-Ching Ho and Walawender (1983), bigger bubble or slug structure has higher rise velocity. Since Gidaspow model produces bigger bubble and slug than De Felice and EHKL models, the bubble rise velocity of Gidaspow model is highest which is in contradiction to the lowest pressure fluctuation frequency predicted by Gidaspow model as shown in Fig. 11 at first glance. Keep in mind that Gidaspow model also gives the largest bed expansion and the fluctuation period is related to the ratio of the expanded bed height to the rise velocity. The lowest fluctuation frequency (i.e. longest period) predicted by Gidaspow model implies that the travelling distance of the bubble dominates its rise velocity for our simulation cases.

### *3.5. Effect of collision parameters e and μ*

In order to study the effect of the two key collision parameters: the restitution coefficient *e*, and the friction coefficient $\mu$, on the fluidization behavior, an ideal-collision case ($e = 1$, $\mu = 0$) is also simulated. Figure 12 shows the snapshots of particle flow patterns for the ideal-collision case at $t = 15$s for the three drag models. Moreover, in the animation of the results it can be observed that, except for the start-up stage ($t$<1s), no bubbling and slugging occur at all and after a vigorous expansion the bed remains rather homogeneously fluidized, which is completely different from the case with non-ideal, more realistic particles ($e = 0.9$, $\mu = 0.3$) as shown in Fig. 8 where a bubble experiences its generation, growth and collapse process periodically. A possible explanation for this phenomenon is depicted in Fig. 13. As shown in Fig. 13, the bed pressure drop $\Delta p$ is almost constant with time in the ideal-collision case, which results in a nearly homogeneous flow structure (constant bed expansion). However, the pressure fluctuation in the non-ideal case is much larger than that in the ideal case, implying that it produces a more heterogeneous flow structure (periodic bubbling). This phenomenonal difference indicates that material properties, as reflected by collision parameters (*e* and $\mu$) have a strong influence on the particle pattern formation. Therefore, real parameters should be chosen in order to obtain realistic fluidization behavior. As also shown in Fig. 12, although all the three drag models predict no bubble and slug formation for the ideal case, the height of the expanded bed is different and Gidaspow model has the largest bed expansion, this feature is consistent with the previous findings in subsection 3.3. It is worth to mention that Hoomans et al. (1996) who adopted a hard-sphere collision model in contrast to our soft-sphere model also reported the same phenomenon as ours for the ideal-collision case, which qualitatively verifies the capacity of our approach.

Author's Post-print version. Article published in Chemical Engineering Science
DOI: doi.org/10.1016/j.ces.2013.03.038
Published version: https://www.sciencedirect.com/science/article/pii/S0009250913002200

Li and Kuipers (2003) explored the effect of non-linearity of the gas drag by altering values of the exponent of the porosity $\varepsilon_g$ in drag correlations. They found that, when increasing the exponent of $\varepsilon_g$, the flow structure displays many modes, ranging from perfectly homogeneous particulate flow with small bed expansion to heterogeneous flow with high bed expansion for ideal-collision case. From Table 1, it is easily observed that the increase of porosity exponent provides a stronger drag force acting on the particles and it will make the bed height increase dramatically. They also reported that the heterogeneous flow structure for ideal-collision case features with looser packing, which differs significantly from the heterogeneous flow structure in non-ideal case (clear bubble or slug formation). The loose packing of particles in the ideal system is attributed to the fact that no energy is dissipated during the frequent particle-particle collisions. This loose-packing feature is in agreement with the phenomenon presented in Fig. 12. Since the conventional values of porosity exponent are kept for each drag model in our work, enhancing exponent of the porosity to produce more heterogeneous flow structure for idea-collision case like Li and Kuipers (2003) did is beyond the scope of this work.

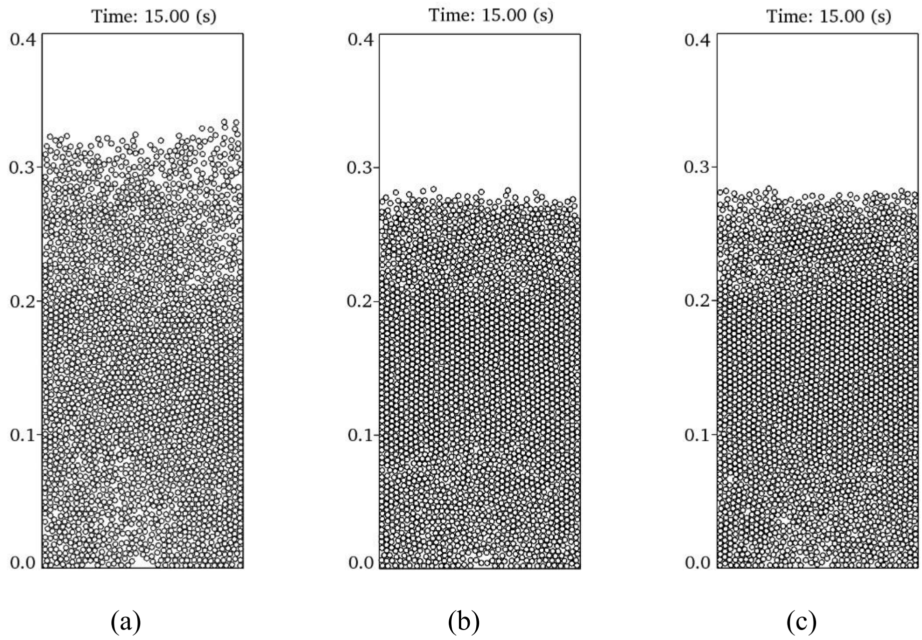


**Fig. 12.** Snapshots of particle flow patterns at $t = 15$ s for ideal-collision case ($e = 1$, $\mu$=0). (a) Gidaspow model; (b) Di Felice model; (c) EHKL model.

Author's Post-print version. Article published in Chemical Engineering Science
DOI: doi.org/10.1016/j.ces.2013.03.038
Published version: https://www.sciencedirect.com/science/article/pii/S0009250913002200

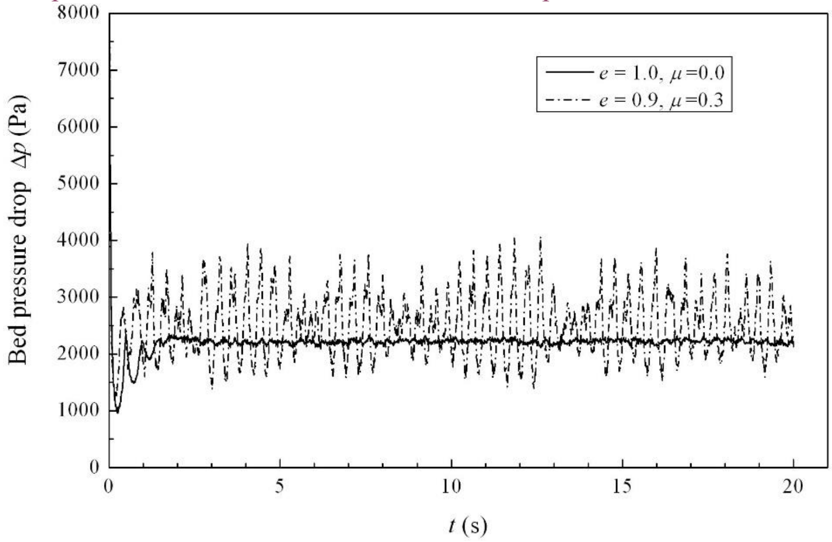


**Fig. 13.** The comparison of bed pressure drop $\Delta p$ between the ideal-collision case ($e$ = 1, $\mu$=0) and the non-ideal collision case ($e$ = 0.9, $\mu$=0.3) for Gidaspow model.

### *3.6. Effect of spring stiffness*

**Table 5**

Simulation results of various spring stiffnesses for the three drag models.

| **Model** | **Spring stiffness $k_n$, (N/m)** | **Mean bed pressure drop, $\overline{\Delta p}$ (kPa)** | **Frequency $f$, (Hz)** |
|---|---|---|---|
| Gidaspow (1994) | $1.28\times10^5$ | 2.51 | ~2.45 |
| | $1.28\times10^6$ | 2.50 | ~2.30 |
| | $1.28\times10^7$ | 2.49 | ~2.20 |
| Di Felice (1994) | $1.28\times10^5$ | 2.54 | ~2.90 |
| | $1.28\times10^6$ | 2.51 | ~2.70 |
| | $1.28\times10^7$ | 2.49 | ~2.65 |
| EHKL (2006) | $1.28\times10^5$ | 2.53 | ~2.80 |
| | $1.28\times10^6$ | 2.52 | ~2.70 |
| | $1.28\times10^7$ | 2.51 | ~2.55 |

The spring stiffness is also a parameter needed to be predetermined for the soft-sphere collision model adopted in this work. As discussed in Section 2.1, using the Hertzian contact theory, the spring stiffness can be calculated from the physical properties such as Young's modulus and Poisson ratio (Tsuji et al., 1992). The previous researchers (Hoomans, 1999; Xu and Yu, 1997; Tsuji et al, 1993) usually assumed that the effect of spring stiffness on particle motion was negligible and a small value ($10^2$~$10^4$) was arbitrarily chosen to save computation time. To test the influence of the spring stiffness, totally 3 runs of simulation are carried out for each drag model, corresponding to the cases with an increasing spring stiffness of one order of magnitude. Table 5 lists the predicted mean pressure drops and fluctuation frequencies. It can be observed that both bed pressure drop and fluctuation frequency decrease as the spring stiffness increases for all the drag models although the variation is small. Therefore if experimental data is available and one aims to improve the agreement between the simulated result and the experimental one, the spring stiffness is also an issue needed to be taken into account. After detailed examinations of the video sequences of the simulations, the effect of the spring stiffness on the fluctuation frequency can be explained as follows. As discussed in section 3.4, the fluctuation frequency is in accordance with the bubbling frequency. With an increase in the spring stiffness, the particles become more rigid and the overlap allowed between them becomes smaller which leads to a particle configuration where the particles are less closely spaced which results in a higher expanded bed. Consequently it will take a rising bubble a little longer time (a lower frequency) to travel through a higher bed.

### *3.7. Effect of the discontinuity in the Gidaspow model*

As mentioned above, the Gidaspow drag model has a discontinuous transition between the Ergun (1952) and Wen and Yu (1966) correlations at a gas volume fraction $\varepsilon_g$ of 0.8. Physically, the drag force is a continuous function of both particle Reynolds number $Re_p$ and $\varepsilon_g$ and therefore drag models should be continuous functions. In order to remove the discontinuity in the Gidaspow model, here, a similar approach to the one used by Leboreiro et al. (2008a) is implemented, namely a linear interpolation over a transition region. The Ergun (1952) expression (denoted by $\beta_E$) for the inter-phase momentum transfer coefficient, is used when $\varepsilon_g$ is below 0.7. If $\varepsilon_g$ is above 0.8, then the Wen and Yu (1966) correlation (denoted by $\beta_{WY}$) is employed. If $\varepsilon_g$ lies in the transition region between 0.7 and 0.8, the following linear interpolation is adopted:

Author's Post-print version. Article published in Chemical Engineering Science
DOI: doi.org/10.1016/j.ces.2013.03.038
Published version: https://www.sciencedirect.com/science/article/pii/S0009250913002200

$$\beta_{\mathrm{TG}} = \beta_{\mathrm{E}} \frac{0.8-\varepsilon_{\mathrm{g}}}{0.1} + \beta_{\mathrm{WY}} \frac{\varepsilon_{\mathrm{g}} - 0.7}{0.1} \tag{9}$$

where $\beta_{\mathrm{TG}}$ is the inter-phase momentum transfer coefficient in the linear transition region for the Gidaspow model. Figure 14 presents the bed pressure drop $\Delta p$ against time $t$ for the original Gidaspow model and the linear continuous one described above. No significant differences are observed in the mean pressure drop and fluctuation frequency between the original Gidaspow model and the continuous one, which is consistent with the findings by Leboreiro (2008b).

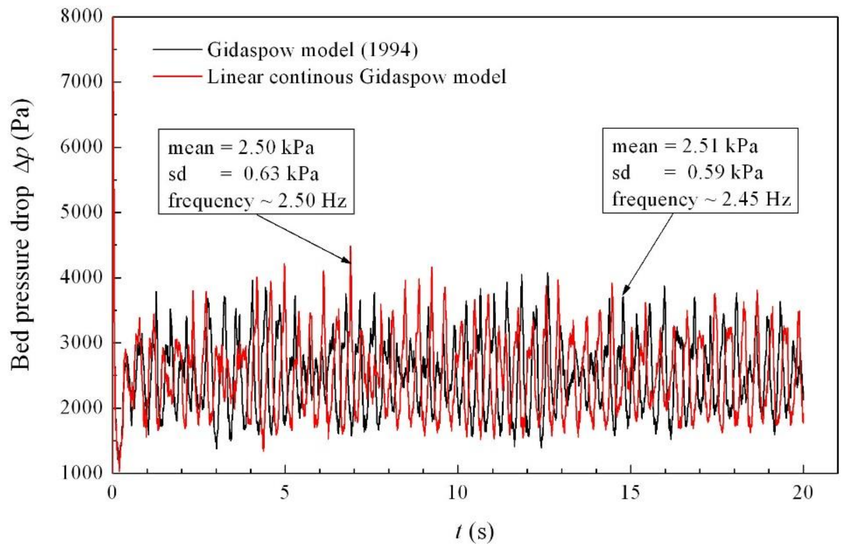


**Fig. 14.** Bed pressure drop $\Delta p$ against time $t$ for Gidaspow model and the linear continuous Gidaspow model.

## 4. Conclusions

Numerical simulations of a bubbling gas-solid fluidized bed reactor have been performed in a pseudo-3D domain using the Eulerian-Lagrangian approach to investigate the effects of three widely used drag correlations on the hydrodynamic behaviors. A soft-sphere model is adopted to resolve the inter-particle and particle-wall collision dynamics. The results have been analyzed in terms of particle flow pattern, bed expansion height, bed pressure drop, and fluctuation frequency. Qualitatively, formation of bubbles and slugs and the process of particle mixing are observed to occur for all the drag models, although the Gidaspow model is found to be most energetic and the Di Felice and EHKL models yield minor difference. Quantitatively, the mean pressure drops predicted by the three models agree quite well with each other and the amplitudes of the fluctuations measured by the standard deviation are also comparable. However, a significant difference in the frequency of pressure fluctuations is found that the Gidaspow model predicts a lowest fluctuation frequency whereas the Di Felice gets a highest one. Considering that there are more than ten drag correlations available in the literature (Esmaili and Mahinpey, 2011; Loha et al., 2012), care must be taken to make a suitable choice for one's particular application.

The effects of restitution coefficient $e$, friction coefficient $\mu$, and spring stiffness $k_n$ on the fluidization behavior are also investigated in this study. It is found that no bubbling and slugging occur at all for the ideal-collision case ($e$ = 1, $\mu$= 0) and that both mean bed pressure drop and fluctuation frequency slightly decrease as the spring stiffness increases for all the three drag models. Finally, the discontinuity in the Gidaspow model is removed by a linear interpolation scheme and no significant differences are observed in the mean bed pressure drop and fluctuation frequency between the original Gidaspow model and the linear continuous model. However, fluidized bed is a huge and very complicated multiphase-flow system, and is affected by many related issues such as container geometry, operational conditions, particle size distribution and material properties. Further modeling efforts are required to study the influence of all these parameters. Moreover, new experimental studies should be carried out using recent advancements in instrumentation engineering in order to compare with our modeling results.

## Acknowledgements

The authors would like to thank partners in CenBio, the BioEnergy Innovation Centre, and GasBio for financial support.

Author's Post-print version. Article published in Chemical Engineering Science
DOI: doi.org/10.1016/j.ces.2013.03.038
Published version: https://www.sciencedirect.com/science/article/pii/S0009250913002200

**References**

Benyahia, S., Syamlal, M., O'Brien, T.J., 2006. Extension of Hill-Koch-Ladd drag correlation over all ranges of Reynolds number and solids volume fraction. Powder Technology 162, 166-174.

Bird, R.B., Stewart, W.E., Lightfoot, E.N., 1960. Transport Phenomena. John Wiley and Sons, New York.

Boyalakuntla, D.S., 2003. Simulation of Granular and Gas-Solid Flows Using Discrete Element Method. Ph.D. thesis, Carnegie Mellon University, Pittsburgh, Pennsylvania.

Cundall, P.A., Strack, O.D.L., 1979. A discrete numerical model for granular assemblies. Geotechnique 29, 47-65.

Deen, N.G., van Sint Annaland, M., van der Hoef, M.A., Kuipers, J.A.M., 2007. Review of discrete particle modeling of fluidized beds. Chemical Engineering Science 62, 28-44.

Di Felice, R., 1994. The voidage function for fluid-particle interaction systems. Int. J. Multiphase Flow 20, 153-159.

Du, W., Bao, X., Xu, J., Wei, W., 2006. Computational fluid dynamics (CFD) modeling of spouted bed: Assessment of drag coefficient correlations. Chemical Engineering Science 61, 1401-1420.

Ergun, S., 1952. Fluid flow through packed columns. Chemical Engineering Progress 48, 89-94.

Esmaili, E., Mahinpey, N., 2011. Adjustment of drag coefficient correlations in three dimensional CFD simulation of gas-solid bubbling fluidized bed. Advances in Engineering Software 42, 375-386.

Gerber, S., Behrendt, F., Oevermann, M., 2010. An Eulerian modeling approach of wood gasification in a bubbling fluidized bed reactor using char as bed material. Fuel 89, 2903-2917.

Gidaspow, D., 1994. Multiphase flow and fluidization. Academic Press, San Diego, USA.

Hill, R.J., Koch, D.L., Ladd, A.J.C., 2001a. The first effects of fluid inertia on flows in ordered and random arrays of spheres. J. Fluid Mech. 448, 213-241.

Hill, R.J., Koch, D.L., Ladd, A.J.C., 2001b. Moderate-Reynolds-number flows in ordered and random arrays of spheres. J. Fluid Mech. 448, 243-278.

Hoomans, B.P.B., 1999. Granular dynamics of gas-solid two-phase flows. Ph.D. thesis, University of Twente, Enschede, The Netherlands.

Hoomans, B.P.B., Kuipers, J.A.M, Briels, W.J., van Swaaij, W.P.M., 1996. Discrete particle simulation of bubble and slug formation in a two-dimensional gas fluidised bed: A hard-sphere approach. Chemical Engineering Science 51, 99-118.

Hoomans, B.P.B., Kuipers, J.A.M. and van Swaaij, W.P.M., 2000. Granular dynamics simulation of segregation phenomena in bubbling gas-fluidised beds. Powder Technology 109, 41-48.

Jung, J. and Gidaspow, D., 2005. Measurement of two kinds of granular temperatures, stresses, and dispersion in bubbling beds. Ind. Eng. Chem. Res. 44, 1329-1341.

Kafui, K.D., Thornton, C., Adams, M.J., 2002. Discrete particle-continuum fluid modelling of gas-solid fluidised beds. Chemical Engineering Science 57, 2395-2410.

Kloss, C., Goniva, C., Aichinger, G., Pirker, S., 2009. Comprehensive DEM-DPM-CFD simulations model synthesis, experimental validation and scalability. In: Seventh International Conference on CFD in the Minerals and Process Industries CSIRO, Melbourne, Australia.

Ku, X., Li, T., Løvås, T., (in press). Eulerian-Lagrangian simulation of a bubbling fluidized bed reactor: Assessment of drag force correlations. Thermal Science.

Leboreiro, J., et al., 2008a. The influence of binary drag laws on simulations of species segregation in gas-fluidized beds. Powder Technology 184, 275-290.

Leboreiro, J., 2008b. Influence of drag laws on segregation and bubbling behavior in gas-fluidized beds. Ph.D. thesis, University of Colorado, Boulder, USA.

Li, J., Kuipers, J.A.M., 2003. Gas-particle interactions in dense gas-fluidized beds. Chemical Engineering Science 58, 711-718.

Lin, J., Shi, X. Yu, Z., 2003. The motion of fibers in an evolving mixing layer. International Journal of Multiphase Flow 29, 1355-1372.

Link, J.M., Cuypers, L.A., Deen, N.G. Kuipers, J.A.M., 2005. Flow regimes in a spout-fluid bed: a combined experimental and simulation study. Chemical Engineering Science 60, 3425-3442.

Loha, C., Chattopadhyay, H., Chatterjee, P.K., 2012. Assessment of drag models in simulating bubbling fluidized bed hydrodynamics. Chemical Engineering Science 75, 400-407.

Oevermann, M., Gerber, S., Behrendt, F., 2009, Euler–Lagrange/DEM simulation of wood gasification in a bubbling fluidized bed reactor. Particuology 7, 307-316.

OpenCFD Ltd, 2011. OpenFOAM-The Open Source CFD Toolbox-User Guide (Version 2.1.0) <http://www.openfoam.org/docs/>.

Papadikis, K., Gu, S., Bridgwater, A.V., Gerhauser, H., 2009. Application of CFD to model fast pyrolysis of biomass. Fuel Processing Technology 90, 504-512.

Su, J., Gu, Z., Xu, X.Y., 2011. Discrete element simulation of particle flow in arbitrarily complex geometries. Chemical Engineering Science 66, 6069-6088.

Taghipour, F., Ellis, N., Wong, C., 2005. Experimental and computational study of gas-solid fluidized bed hydrodynamics. Chemical Engineering Science 60, 6857-6867.

Tho-Ching Ho, L.T.F., Walawender, W.P., 1983. Measurements of the rise velocities of bubbles, slugs and pressure waves in a gas-solid fluidized bed using pressure fluctuation signals. AIChE Journal 29, 33-39.

Tsuji, Y., Tanaka, T., Ishida T., 1992. Lagrangian numerical simulation of plug flow of cohesionless particles in a horizontal pipe. Powder Technology 71, 239-250.

Tsuji, Y., Kawaguchi, T., Tanaka, T., 1993. Discrete particle simulation of two-dimensional fluidized bed. Powder Technology 77, 79-87.

van der Hoef, M.A., Beetstra, R., Kuipers, J.A.M., 2005. Lattice-Boltzmann simulations of low-Reynolds-number flow past mono- and bidisperse arrays of spheres: results for the permeability and drag force. J. Fluid Mech. 528, 233-254.

Wang, J., van der Hoef, M.A., Kuipers, J.A.M., 2009. Why the two-fluid model fails to predict the bed expansion characteristics of Geldart A particles in gas-fluidized beds: a tentative answer. Chemical Engineering Science 64, 622–625.

Wen, C.Y., Yu, Y.H., 1966. Mechanics of Fluidization. Chemical Engineering Progress Symposium Series 62, 100-111.

Xu, B.H., Yu, A.B., 1997. Numerical simulation of the gas-solid flow in a fluidized bed by combining discrete particle method with computational fluid dynamics. Chemical Engineering Science 52, 2785-2809.

Zhou, Z.Y., Zhu, H.P., Yu, A.B., Wright, B., Zulli, P., 2008. Discrete particle simulation of gas-solid flow in a blast furnace. Computers and Chemical Engineering 32, 1760-1772.